Pathological transitions in myelin membranes driven by environmental and multiple sclerosis conditions

Rona Shaharabani[a,b], Maor Ram-On[c,d], Yeshayahu Talmon[c,d], and Roy Beck[e,1]

[a]School of Chemistry, Tel Aviv University, Tel Aviv 6997801, Israel; [b]The Center for Nanoscience and Nanotechnology, Tel Aviv University, Tel Aviv 6997801, Israel; [c]Department of Chemical Engineering, Technion–Israel Institute of Technology, Haifa 3200003, Israel; [d]Russell Berrie Nanotechnology Institute, Technion–Israel Institute of Technology, Haifa 3200003, Israel; and [e]School of Physics and Astronomy, Tel Aviv University, Tel Aviv 6997801, Israel

Edited by David A. Weitz, Harvard University, Cambridge, MA, and approved September 18, 2018 (received for review March 12, 2018)

Multiple sclerosis (MS) is an autoimmune disease, leading to the destruction of the myelin sheaths, the protective layers surrounding the axons. The etiology of the disease is unknown, although there are several postulated environmental factors that may contribute to it. Recently, myelin damage was correlated to structural phase transition from a healthy stack of lamellas to a diseased inverted hexagonal phase as a result of the altered lipid stoichiometry and low myelin basic protein (MBP) content. In this work, we show that environmental conditions, such as buffer salinity and temperature, induce the same pathological phase transition as in the case of the lipid composition in the absence of MBP. These phase transitions have different transition points, which depend on the lipid's compositions, and are ion specific. In extreme environmental conditions, we find an additional dense lamellar phase and that the native lipid composition results in similar pathology as the diseased composition. These findings demonstrate that several local environmental changes can trigger pathological structural changes. We postulate that these structural modifications result in myelin membrane vulnerability to the immune system attacks and thus can help explain MS etiology.

myelin | multiple sclerosis | lamellar to hexagonal phase transition | SAXS | cryo-TEM

Myelin sheaths, multilayered stacked membranes, act as an electrical insulator surrounding the neuron's axon (1–4). Their structure is crucial for fast and efficient conduction of nerve impulses (5–8). Multiple sclerosis (MS) is a chronic inflammatory autoimmune disease resulting in myelin destruction and neural dysfunction (5, 9–13). Together with its animal model (14), experimental autoimmune encephalomyelitis (EAE), MS is characterized by the appearance of lesions, reflecting loss of membrane adhesion, swelling across the water gaps, vacuolization, vesiculation, and eventual disintegration of the myelin structure (15). MS is also manifested by a wide range of clinical symptoms and varying disease courses among patients (11). The etiology of MS is still unknown, and currently there is no cure for the disease (2, 13).

Recent in vitro and in vivo experiments (16) addressed the structural consequences of lipid stoichiometry modifications (11, 17–21) in normal (i.e., native) and diseased (i.e., modified) states (*SI Appendix*, Table S1). In physiological buffer environment, native lipid composition results in multilamellar structures (L_α), suitable for myelin function, while modified composition is structurally different with coexisting L_α and 2D inverted hexagonal phase (H_{II}) (16). This phase transition was further discussed in the context of a possible trigger for the outbreak of the MS disease. In the process of transitioning to H_{II}, the membrane undulates with large local curvature. Such undulations induce spontaneous pores, resulting in a vulnerability of the membrane to an attack by the immune system.

Environmental conditions are highly regulated in vivo. Nevertheless, the membrane's proximity to a structural phase transition boundary makes it susceptible to minor local environmental alterations. Since the membrane's vulnerability is the disease's possible cause, finding such conditions that alter the structure is of great importance and thus are investigated here.

To study myelin vulnerability, we measure its structure in the context of membrane self-assembly, which has been widely studied experimentally and theoretically for the past half a century (22). From a physical perspective, the competing forces between the lipids determine the nanoscopic structure and the macroscopic mesophase. The lamellar to inverted hexagonal phase transition can be induced by various means, among them temperature, buffer salinity, and pH (22–26), as detailed in *SI Appendix*, section 1.

Since the environmental conditions regulate the intermolecular forces between the lipids, the nanoscopic detailed structure, such as membrane unit cell length, can also vary. Therefore, by measuring the structures at various conditions, it is possible to identify the dominant intermolecular forces stabilizing the membranes. For example, the Derjaguin–Landau–Verwey–Overbeek (DLVO) theory correlates the membrane separation distance to the van der Waals and electrostatic interactions between the membrane leaflets (27–34). The DLVO theory has been validated for simple homogeneous membranes and for monovalent salt buffer (27), and results in the free energy per unit area of the following:

Significance

In demyelination diseases, such as multiple sclerosis, the structure of the axons' protective sheaths is disrupted. Due to the proximity of cytoplasmic myelin membrane to structural phase transition, minor alterations in the local environmental conditions can have devastating results. Using small-angle X-ray scattering and cryogenic transmission electron microscopy, we show that drastic structural reorganization and instabilities of myelin membrane are linked to specific environmental conditions and molecular composition in healthy and diseased states. These instabilities involve phase transition from the healthy lamellar membranes to pathological inverted hexagonal phase. These results highlight that local environmental conditions are critical for myelin function and should be considered as alternative routes for early pathology and as a means to avoid the initiation of demyelination.

Author contributions: R.S. and R.B. designed research; R.S., M.R.-O., Y.T., and R.B. performed research; R.S., M.R.-O., Y.T., and R.B. contributed new reagents/analytic tools; R.S., M.R.-O., Y.T., and R.B. analyzed data; and R.S., Y.T., and R.B. wrote the paper.

The authors declare no conflict of interest.

This article is a PNAS Direct Submission.

[1]To whom correspondence should be addressed. Email: roy@tauex.tau.ac.il.

This article contains supporting information online at www.pnas.org/lookup/suppl/doi:10.1073/pnas.1804275115/-/DCSupplemental.

Published online October 15, 2018.

$$f_{\text{tot}} = \frac{2\lambda_D k_B T}{\pi l b^2} e^{-d_W/\lambda_D} - \frac{A}{12\pi}\frac{1}{d_W^2}. \quad [1]$$

Here, λ_D is the Debye screening length, inversely proportional to the square root of the salt concentration; l is the Bjerrum length, describing the distance at which two elementary charges with an energy of $k_B T$ interact; d_W is the distance between two leaflets; b is the Gouy–Chapman length, inversely proportional to the membrane surface charge density (σ); and A is the Hamaker constant (27, 28, 30). The equilibrium membrane spacing (d_L), accessible by small-angle X-ray scattering (SAXS), is related to the bilayer thickness (d_b) and the water layer gap (d_W) by the following: $d_L = d_W + d_b$. By minimizing the free energy with respect to the separation, $\partial f(d_L)/\partial d_L = 0$, a direct relation between the interlamellar spacing and salt concentration is found. Unfortunately, the ordinary DLVO theory cannot explain results for high divalent salt concentrations (e.g., calcium and magnesium) even with additional components, such as hydration forces (27). The electrostatic interaction term should take into account either constant charge, constant potential, or charge regulation boundary conditions. Because in our case $d_W \gg \lambda_D$, there is no actual difference between those cases and Eq. **1** holds (34).

In this study, we show the structural implication of environmental alteration on the cytoplasmic myelin membrane structure. Specifically, we demonstrate that changes in buffer salinity (ion type and concentration, C) or in temperature cause the membrane to make a transition between a healthy stack of lamellas to inverted hexagonal phase. The phase transition points (e.g., T^*, C^*) are ion specific and strongly depend on the membrane composition, which should be of great relevance to myelin stability and vulnerability, and in particular in the diseased state.

Results and Discussion

In this study, we conducted experiments on a model membrane system containing the lipid composition of the cytoplasmic myelin membrane in native and modified states (16, 17) (*SI Appendix*, Table S1) at altered environmental conditions. The self-assembly structures were studied by SAXS and cryogenic transmission electron microscopy (cryo-TEM). At physiological conditions (10 mM Mops, 150 mM NaCl, and 2 mM $CaCl_2$, pH of 7.4), previous studies showed that in the absence of myelin basic protein (MBP) the native lipid composition exhibits a multilamellar phase (L_α), with an interlamellar spacing of $d_L = 113$ Å, while the modified composition showed a coexisting of an L_α ($d_L = 123$ Å) and an inverted hexagonal phase (H_{II}) phase with unit cell length of $a_H = 90$ Å. The unit cell dimensions are directly measured from the SAXS correlation peaks positions. Multilamellar and hexagonal mesophases reflections result in $q_L(00n) = 2\pi n/d_L$ and $q_H(hk) = 4\pi\sqrt{k^2 + h^2 + hk}/\sqrt{3a_H{}^2}$, respectively. Here, q is the scattering wave-vector, and n, h, and k are Miller indices; d_L and a_H represent the real-space unit cell spacing in each phase.

First, we examined the structure of the cytoplasmic myelin membrane, while changing the monovalent ion entity and keeping the overall ionic strength as in the physiological case, for comparison. It is important to study the effect of replacing sodium with potassium ions because both are needed for the generation of nerve impulses and for maintenance of the electrolyte and fluid balance.

Interestingly, we find distinguishable differences between the self-assembly structures of native and modified lipid compositions in the presence of either 150 mM NaCl or KCl (*SI Appendix*, Fig. S1 *A* and *B*). Here, neither cation alters the dominant nanoscale structures of each lipid compositions (i.e., L_α or L_α and H_{II}); nevertheless, the unit cell lengths depend on the cation type. For the modified lipid composition (*SI Appendix*, Fig. S1*A*), the hexagonal unit cell lengths are rather similar with $a_H(K^+) = 95$ Å $> a_H(Na^+) = 90$ Å. Coexisting with the inverted hexagonal phase, we find a lamellar phase with unit cell spacing of $d_L(Na^+) = 123$ Å $> d_L(K^+) = 115$ Å. For the native lipid composition (*SI Appendix*, Fig. S1*B*), a dominant lamellar phase is clearly present for both cations, with similar unit cell dimensions [$d_L(K^+) = 114$ Å $\sim d_L(Na^+) = 113$ Å]. For the KCl case, we find two additional correlation peaks with unit cell lengths of $2\pi/q = 67$ and 64 Å. These correlation lengths correspond to that found for cholesterol aggregates (35) and to "denser lamellar phase" that will be discussed later.

To examine further the ion-type specificity, we measured the effect of different divalent ions on the self-assembled mesophases. Here, the effect is much more dominant than those of the monovalent ions. Calcium ions play an important role in signal transduction pathways. Calcium acts as a secondary messenger in neurotransmitter release from neurons, and is important for maintaining the potential difference across excitable cell membranes (3, 36). Zinc is known to control the MBP, the key protein in the myelin sheath, which acts as an intermolecular adhesion protein, binding the two cytoplasmic membranes of the myelin (37). Zinc and calcium are chemically similar, having the same oxidation state, but they have different biological roles and functions.

Calcium and magnesium give the same structure for native and modified lipid compositions (*SI Appendix*, Fig. S1 *C* and *D*). The unit cell length depends on the cation type: for the native lipid composition (*SI Appendix*, Fig. S1*D*), $d_L(Mg^{2+}) = 122$ Å $> d_L(Ca^{2+}) = 113$ Å; for modified lipid composition (*SI Appendix*, Fig. S1*C*), $d_L(Mg^{2+}) = 127$ Å $\geq d_L(Ca^{2+}) = 123$ Å; and for the coexisting inverted hexagonal phase unit cell length, $a_H(Mg^{2+}) = 113$ Å $> a_H(Ca^{2+}) = 90$ Å.

With zinc, there are structural changes for both lipid compositions (*SI Appendix*, Fig. S1 *C* and *D*). First, the native composition (*SI Appendix*, Fig. S1*D*) exhibits coexistence of lamellar and inverted hexagonal phase. Second, for both lipid compositions, we find a new phase that we denote the "dense lamellar phase," with unit cell lengths of $d_d = 2\pi/q = 84$ Å, 66 Å (for modified and native compositions, respectively). Note that, at physiological $ZnCl_2$ concentration, the native composition shows the same characteristics as the diseased state, with coexistence of lamellar and hexagonal phases.

Comparing the three divalent cations, we find that in the modified lipid composition the inverted hexagonal unit cell lengths are ion specific: $a_H(Mg^{2+}) > a_H(Ca^{2+}) > a_H(Zn^{2+})$. Similarly, the lamellar phase unit cell length for both lipid compositions follows: $d_L(Mg^{2+}) \geq d_L(Ca^{2+}) > d_L(Zn^{2+})$ for modified and native lipid compositions.

The concentration of the ions mentioned above can vary globally and locally. Cation concentration may change during diseased state (38–42) and locally can be either very low or high. More importantly, varying the cation concentration can highlight differences between the cation's role in modifying the membrane structure. These local changes in concentration may result in dramatic structural variations that can affect the integrity and the stability of the structure. Hence, we examined separately the effect on the mesophase structure of changing the concentration of all of the monovalent and divalent ions mentioned.

Using SAXS, we studied the changes in monovalent ions concentration between 0 and 500 mM (*SI Appendix*, Fig. S2), and found that for both lipid compositions, and both monovalent ions, the lamellar phase unit cell spacing decreases (Fig. 1, red squares). For the modified lipid composition, the hexagonal phase increases until it reaches a saturation at 200 mM NaCl and 150 mM KCl to $a_H = 101$ and 95 Å, respectively (Fig. 1 *A* and *C*). At low monovalent salt concentration, the lamellar phase is not ordered, as can be seen from the SAXS data (*SI Appendix*, Fig. S2), where the lamellar correlation peaks are broad (Fig. 1 *A* and *B*, red unfilled squares). In addition to the coexisting lamellar and inverted hexagonal phases, and above a transition concentration (C^*), we find correlation peaks that we attribute to cholesterol aggregations (*SI Appendix*, Fig. S2 *C* and *D*) (16, 35). Notably, the cholesterol correlation peak, with unit cell length of about 65 Å, appears in almost all KCl concentrations, suggesting that KCl enhances the nucleation of cholesterol crystalline domains within the membrane. The mechanism supporting these results requires further investigation. Surprisingly, above 250 mM

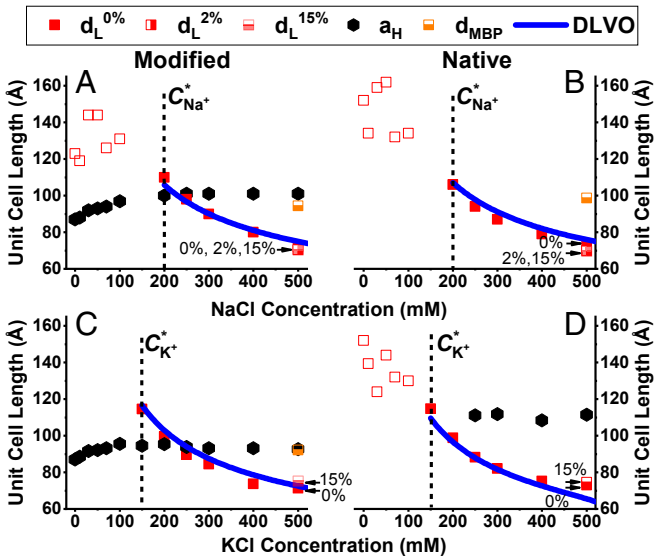

Fig. 1. Unit cell lengths (d_L and a_H) for increasing monovalent salt concentrations. (*A*–*D*) Modified (*A* and *C*) and native (*B* and *D*) lipid compositions unit cell length at increasing NaCl (*A* and *B*) and KCl (*C* and *D*) concentrations from 0 to 500 mM. The solid line is a DLVO fitting using Eq. **1**. In *B*, the only free parameter is the Hamaker constant, while in *A*, *C*, and *D* the free parameter is the surface charge, σ, using the same Hamaker constant from 1B fit. The unfilled symbols represent an unordered phase. The dotted lines indicate the monovalent ions' transition concentration, C^*. Samples with low (2 wt%) and high (15 wt%) MBP content are marked with half-filled symbols. The additional lamellar phase in the presence of 15 wt% MBP is denoted as d_{MBP} (orange squares).

KCl concentration, the native lipid composition exhibits coexistence of lamellar and hexagonal phases (Fig. 1*D* and *SI Appendix*, Fig. S2*D*), as in the modified lipid composition and physiological buffer conditions.

When changing the monovalent ion type or its concentration, structural changes are seen above a specific concentration, for both native and modified lipid compositions. For both ions at the native lipid composition, below the transition concentration (C^*) we find SAXS signal with broad correlation peaks, indicating unordered lamellar phase (unfilled squares in Fig. 1 and *SI Appendix*, Fig. S2). Above C^*, the SAXS correlation peaks become prominent as the lamellar phase becomes more ordered (solid squares in Fig. 1 and *SI Appendix*, Fig. S2). The lamellar phase unit cell length decreases with increasing concentration of both monovalent ions, and both lipid compositions. We fit the experimental data to the DLVO theory (Eq. **1**), for the lamellar phase in NaCl, above C^*. The mean area per lipid molecule is taken as ~0.4 nm^2, and the surface charge density of $e^-/(5.7\ \text{nm}^2)$ following Min et al. (17). Being the only unknown parameter, we can now extract the Hamaker constant, which we find to be $A = 22$ zJ. This value agrees well with theoretical and experimental measurements in lipid membranes (31, 43).

Using the same Hamaker constant, we can now find the surface charge density of the lamellar phase at the other compositions. These values might change because specific lipid types might migrate to the different coexisting phases. Therefore, by finding the membrane surface charge, σ, we can compare the amount of the negatively charged lipid, phosphatidylserine (PS), in the lamellar mesophase. For the modified lipid composition with sodium salt, the surface charge density is $e^-/(5.9\ \text{nm}^2)$, a slight decrease from the native monophase. This means that the percentage of the negatively charged lipid is $f \sim 6.8\%$. In the case of potassium salt, the native and modified lipid compositions surface charge densities are found to be $e^-/(7.0\ \text{nm}^2)$ and $e^-/(8.9\ \text{nm}^2)$, respectively. Here, we assume that the average area per lipid molecule does not change significantly when changing the ion type. This indicates that the percentage of the negatively charged lipids is $f \sim 5.7\%$ and 4.5%, respectively. We notice that these negatively charge lipid percent values are lower in the potassium buffer than in the sodium one, which indicates that PS distribution is ion-type sensitive. Moreover, the small difference between the charged lipids in the original native and modified lipid compositions (0.4 mol%, *SI Appendix*, Table S1) cannot explain the rather significant differences between the effective charge densities found here. These results indicate that nonhomogenous distribution of the lipids is present in the coexisting mesophase cases.

While the lamellar phase unit cell length (d_L) condenses with increasing monovalent salt concentration, the hexagonal phase unit cell length (a_H) shows an opposite trend. In particular, we find that, for the modified lipid composition, a_H increases slightly with increasing monovalent salt concentration. This phenomenon occurs for both salts and persists until C^*, at which point a_H becomes salt independent, and the lamellar phase is well ordered (Fig. 1 *A* and *C*). For the native lipid composition, in the presence of potassium ions (Fig. 1*D*), the hexagonal phase appears above C^*, and a_H remains constant with increasing salt concentration.

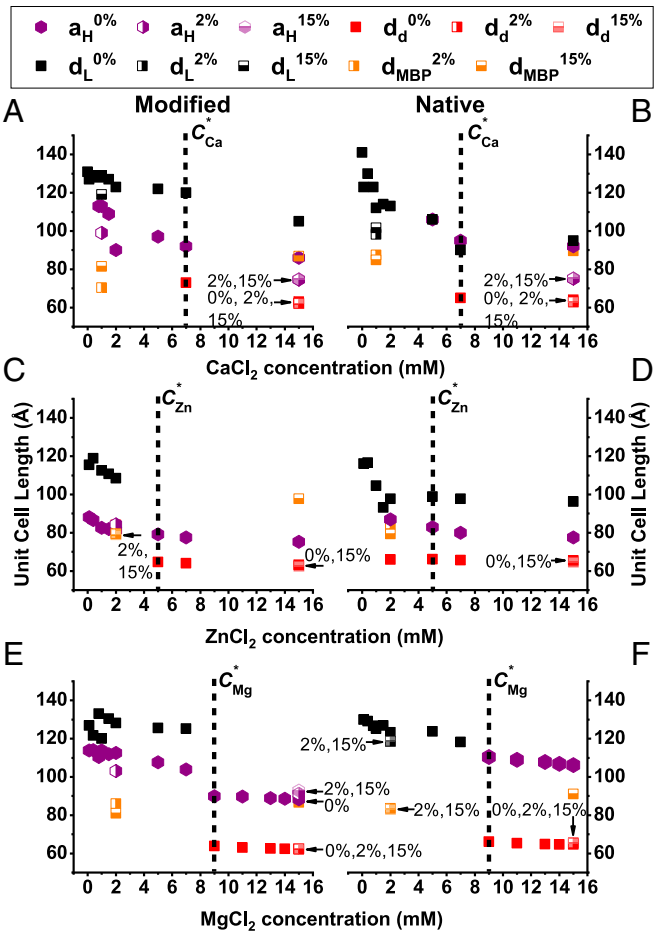

Fig. 2. Unit cell lengths at increasing divalent salt concentrations. (*A*–*F*) Modified (*A*, *C*, and *E*) and native (*B*, *D*, and *F*) lipid compositions' unit cell length at increasing $CaCl_2$ (*A* and *B*), $ZnCl_2$ (*C* and *D*), and $MgCl_2$ (*E* and *F*) concentrations from 0 to 15 mM. The transition concentrations (C^*) are marked with the vertical black dotted lines. The black squares represent the dominant lamellar phase (d_L), the purple hexagonal symbols represent the inverse hexagonal phase (a_H), and the red squares represent the dense lamellar phase (d_d) for all ion types. The additional lamellar phase in the presence of 2 and 15 wt% MBP are denoted as d_{MBP} (half-filled orange squares).

The expansion followed by a saturation of a_H with increasing salt concentration cannot be explained by the DLVO theory. One possible explanation for the expansion can be that ions adsorb onto the hexagonal phase lipids, rather than screen the electrostatic repulsion. These results of charge inversion were previously discussed for charged membranes (44–46). Alternatively, the expansion could be a result of redistribution of the charged lipids between the two phases, and a_H remains constant when the lamellar phase is well ordered.

Next, we evaluated the effect of the divalent ions on the structure of the cytoplasmic myelin membrane, while keeping NaCl salt concentration constant at 150 mM (Fig. 2). Here, as in the monovalent salt case, the lamellar unit cell spacing decreases with increasing divalent salt concentration. In contrast to the previous case, the coexisting hexagonal phase also compacts with elevated salt concentrations. In addition, at higher divalent salt concentrations, another lamellar phase is clearly noticeable with sharp SAXS correlation peaks (*SI Appendix*, Fig. S3). This denser lamellar phase ($d_d \sim 64$ Å) (Fig. 3) is coexisting with the lamellar phase and is also noticeable in the cryo-TEM images (Fig. 3 *B* and *E*). Above the transition concentration, C^*, the hexagonal phase, the lamellar phase (if present), and the dense lamellar phase unit cell lengths remain constant. This phenomenon can also be explained by redistribution of the lipids between the different phases below C^*. Driving forces for the dense phase can be membrane undulation and ion–ion correlations effects that are known to drive attraction between like-charge membranes (28, 47, 48).

For modified lipid composition, the coexistence of lamellar and inverted hexagonal phases differs in the unit cell lengths sizes at saturation $a_H(Mg^{2+}) \gtrsim a_H(Ca^{2+}) > a_H(Zn^{2+})$. Like the modified lipid composition, the native lipid composition exhibits coexisting lamellar and inverted hexagonal phases above the transition concentration, C^*. Again, the hexagonal unit cell lengths differ in size $a_H(Mg^{2+}) > a_H(Ca^{2+}) > a_H(Zn^{2+})$. The transition concentrations follow the trend of the following: $C^*_{Zn^{2+}} = 5$ mM $< C^*_{Ca^{2+}} = 7$ mM $< C^*_{Mg^{2+}} = 9$ mM. The dense lamellar phase has the same unit cell length for all ion types and lipid composition around $d_d \sim 64$ Å. In contrast to the other cations, zinc exhibit a dense lamellar phase at lower concentration before saturating at C^* (Fig. 2 *C* and *D*).

For both lipid compositions, we find that the structural reorganization with divalent ions is different in calcium to that found in zinc or magnesium. In particular, at low calcium concentrations (below 5 mM), the lamellar phase is not well organized as with the other cations (*SI Appendix*, Fig. S3). Interestingly, the concentration for the transition to the condensed lamellar phase does not follow the trend of cation size. One reason could be that the calcium ions adsorb onto the lipid membrane differently (49–52) than magnesium and zinc, although all bear the same charge.

Apart from lipids, native myelin sheaths are rich in proteins, in particular MBP (*SI Appendix*, section 2). MBP presence was previously found to be critical for proper function and structure of myelin (16, 37, 53, 54), since high content completely abolishes the inverted hexagonal phase (16). Regardless of the ion type and lipid compositions, we find that MBP addition competes with the presence of inverted hexagonal phase (Figs. 1 and 2 and *SI Appendix*, Fig. S4), although does not significantly change the unit cell spacings (Figs. 1 and 2). One exception is the modified lipid composition with high $MgCl_2$ concentration where even 15 wt% of MBP does not eliminate the inverted hexagonal phase. In other cases, lower MBP content results in reduction of the hexagonal phase presence, as indicated by lower correlation peaks intensities. Moreover, in high salt and MBP concentrations, we find an additional coexisting lamellar phase with spacing of about $d_{MBP} = 90$ Å (Figs. 1–3 and *SI Appendix*, section 2 and Figs. S4 and S5). At low salt concentration, this lamellar phase can be identified at lower MBP content (2 wt%). Such spacing sustains a water layer thickness matching the dimensions previously estimated for MBP (16, 55).

Another important parameter governing intermolecular forces and interactions between macromolecules is temperature. For example, at elevated temperature, the lamellar to hexagonal phase transition has been demonstrated for single and binary lipids mixtures (24, 56–58). The origin of this thermotropic phase transition is the added mobility of the hydrocarbon chains at elevated temperatures, leading to larger spontaneous curvature (23, 59). The contribution of hydrocarbon chains' entropy to the free energy increases with temperature. As more hydrocarbon chains' conformation is available, the membrane thickness decreases to reduce the interfacial area between the aqueous solution and the lipid hydrocarbon chains (59). Moreover, temperature has an additional effect on the intermolecular forces between the water molecules. That, in turn, changes the effective hydrophobic interaction and the water layer ordering nearby the lipid bilayer (60). Interestingly, previous studies demonstrated that MS episodes are correlated with patients' high fever, although the origin of that effect is still obscure (61, 62).

In Fig. 4, we show the implication of elevated temperature for both lipid compositions. Indeed, structural changes are manifested

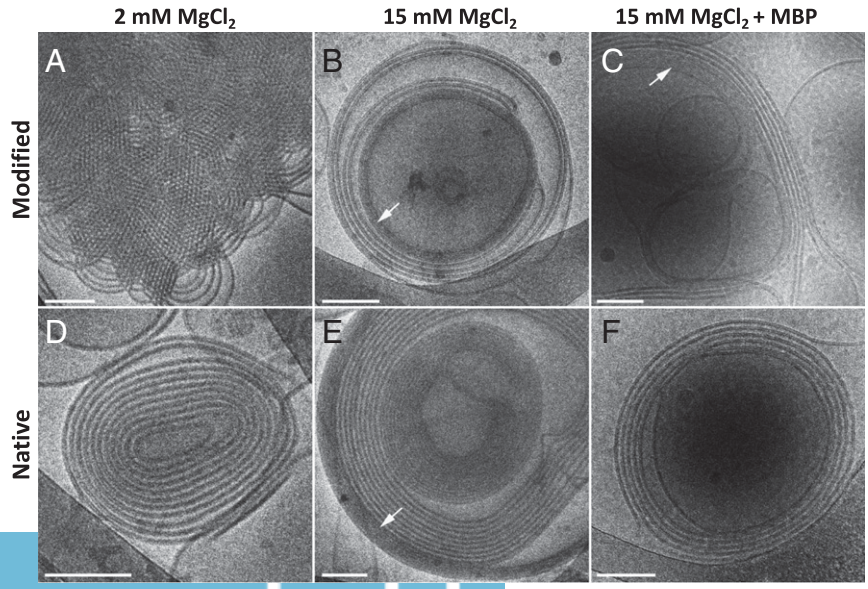

Fig. 3. Native and modified lipid compositions in 2 mM $MgCl_2$, 15 mM $MgCl_2$, and 15 mM $MgCl_2$ with 20 wt% MBP. Cryo-TEM images of modified lipid composition (*A*–*C*) and native lipid composition (*D*–*F*) in the presence of 2 mM $MgCl_2$ (*A* and *D*) or 15 mM $MgCl_2$ with/without 20 wt% MBP (*C* and *F*, and *B* and *E*), respectively. The images show multilamellar vesicles (*B*–*F*) and inverted hexagonal phase (*A*). The dense lamellar phase is indicated by the white arrows. (Scale bars: 100 nm.)

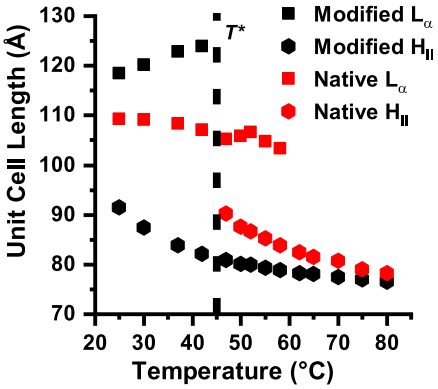

Fig. 4. Native and modified unit cell lengths (d_L and a_H) changes with temperature. Unit cell length of H_{II} (hexagonal symbols) and L_α (squares) of native (red) and modified (black) lipid compositions at increasing temperature from 25 to 80 °C. The transition temperature is denoted by the vertical black dotted line (T^*).

for both lipid compositions. The coexistence of lamellar and inverted hexagonal phases, in the modified lipid composition, changes into a singular inverted hexagonal phase around $T^* =$ 42 °C (*SI Appendix*, Fig. S6). Around the same temperature, the one lamellar phase, in the native lipid composition, changes to coexistence of lamellar and inverted hexagonal phases (Fig. 4, vertical black dotted line). This coexisting region terminates at $T =$ 60 °C, where the system fully transitions into a single inverted hexagonal phase (*SI Appendix*, Fig. S6).

For both lipid compositions, the inverted hexagonal phase unit cell lengths, a_H, decrease with increasing temperature (Fig. 4, hexagonal symbols). Such behavior was previously demonstrated for several simplified lipid systems; it presumably originates from changing the lipids packing parameter (i.e., the ratio between the headgroup size and the hydrocarbon chains projected area) at elevated temperatures (23, 24). In addition, the hydrocarbon chain conformation is considerably more disordered in the H_{II} phase, compared with the L_α phase, which reduces the unit cell length even further (24). Nevertheless, while the lamellar phase unit cell length, d_L (Fig. 4, square symbols) decreases with increasing temperature for the native lipid composition, we find it to increase for the modified lipid composition before disappearing at T^* (Fig. 4, vertical black dotted line). The difference in the temperature trend of d_L suggests that specific molecular forces, attributed to different lipid compositions rearrangement, are important during this phase transition.

As previously mentioned, in the presence of MBP, the modified lipid composition resembles that of native composition without MBP with a singular lamellar phase (16). We find that the temperature dependence of modified lipid composition with high content of MBP shows similar trend to native lipid composition, with elevated T^* of about 60 °C (*SI Appendix*, Fig. S7).

As described in *SI Appendix*, section 1, phosphatidylethanolamine (PE) prefers to form inverted hexagonal phase (23, 31, 63). Cholesterol molecules can also segregate from the lamellar into the hexagonal phase. That will decrease the spacing between adjacent tubes in the hexagonal phase (a_H), as the cholesterol settles between the lipids hydrocarbon chains (64). Following, the hydrocarbon chain packing stress will be relieved by filling the gaps between the cylinders. As a result, stronger van der Walls interactions between the hydrocarbon chains will reduce the unit cell length in the hexagonal arrangement (Fig. 4, hexagonal symbols). Cholesterol segregation can also explain the d_L increase for the modified lipid composition (Fig. 4, black squares). The native lipid composition $d_L(T)$ shows an opposite trend (Fig. 4, red square symbols). Previous studies had shown such behavior, explained by a decrease in the membrane thickness (d_b) with increasing temperature (59). The different trends can be explained by the formation of a mixed phase at modified lipid composition, and a single lamellar phase at the native lipid composition.

Summary

Myelin membrane is a complex biological system having a mixture of different lipids. The cytoplasmic leaflets of myelin contain five dominant components that alter in demyelination diseases. We are able to gain physical understanding of its self-assembled structure with minimal simplifications due to its repeating structure and relatively small number of components.

In our experiments, we find several factors that tend to destabilize the lamellar phase and induce the formation of inverted hexagonal phase. First, changes in the lipid composition and low MBP concentration, as observed by MS pathology, result in L_α to H_{II} phase transition. Inverted hexagonal phase is induced by concentration increase in PS, PE, and mainly cholesterol, and decrease in sphingomyelin (SM) and phosphatidylcholine (PC) lipids. Similarly, ion type and salt concentration are also key factors affecting the lipid organization. We find that increasing the salt concentration, above a transition concentration C^*, destabilizes the lamellar phase and transforms the membrane into the inverted hexagonal phase. For monovalent salts (NaCl and KCl), the transition concentration is above 150 mM, while for divalent salts ($MgCl_2$, $ZnCl_2$, and $CaCl_2$) it is 5–9 mM. This makes the structural phase transition relevant to the biological context, because such concentrations, and in particular local fluctuations to such values, are common in vivo.

Moreover, at high divalent salt concentrations, a dense lamellar phase coexists with the inverted hexagonal phase. Verified by cryo-TEM and SAXS, once formed, the dense lamellar phase has an interlamellar spacing of 64 Å, which leaves about 15-Å thicknesses of water between the bilayers. Importantly, the water layer in the dense lamellar phase is much smaller than the needed space (35 Å) for the adhesive MBP normally placed between the cytoplasmic lipid bilayers. Following, at high MBP concentration, an additional lamellar phase is present with sufficient intermembranal space (~40 Å). In the absence of MBP and at low salt concentration, the lamellar phase spacing decreases with increasing salt concertation, as expected for electrostatic screening. However, once induced, the dense lamellar phase spacing remains constant with further increase in the salt concentration or MBP content.

The transition to the inverted hexagonal phase can be induced by elevated temperatures. Again, the transition temperature is physiologically relevant (42 °C), especially for healthy lipid composition, where the inverted hexagonal phase is normally absent. Moreover, the presence of MBP is shown to protect the membrane from transitioning to the inverted hexagonal phase at physiologically relevant temperatures.

Our results emphasize that minor alterations of the environmental conditions can drive structural instabilities and the formation of the H_{II} phase from the L_α native functional phase. Generally, lower salinity and low temperature are favorable for healthy lamellar phase up to about physiological condition. However, since structural phase transition depends also on the myelin lipid composition, local inhomogeneity in the membrane can have devastating outcomes. We showed that healthy lipid composition is on the verge of a structural phase transition. Due to this proximity to the phase boundary, small local changes can locally change the membrane to another phase. This eventually may lead to vulnerability of the membrane and neuronal dysfunction.

These results are directly connected to MS etiology and diagnostics. Changes in the local environment of the axon, whether by ion type or ion concentration, result in the pathological phase transition that characterizes the diseased state. Further instabilities can be induced at elevated temperature. By evaluating and controlling the environmental conditions, one can stabilize the lamellar phase and avoid the inverted hexagonal phase formation.

Material and Methods

Brain lipids compositions were prepared at desired mole ratios (*SI Appendix*, Table S1). SAXS experiments were carried out in home-built apparatus and

synchrotrons at room temperature and at elevated temperatures. Cryo-TEM samples were prepared using a controlled environment vitrification system at 25 °C and 100% relative humidity. As detailed in *SI Appendix*, section 4.

ACKNOWLEDGMENTS. We are grateful to Philip Pincus, Adrian Parsegian, Michael Kozlov, Michael Schick, and Rudi Podgornik for useful and enlightening conversations. We are thankful for SAXS beamlines for the SAXS measurements: I22 at Diamond Light Source (Oxfordshire, United Kingdom) and I911-SAXS at MAX IV Laboratory (Lund, Sweden). R.S. thanks Eti Malka-Gibor, Micha Kornreich, Yoni Messica, and Ram Avinery for their assistance with the measurements, and Lilah Inzelberg for her help with the programming work. The work was supported by the Israel Science Foundation (571/11 and 550/15) and the Sackler Institute for Biophysics and the Abramson Center for Medical Physics at Tel Aviv University. Travel grants to the synchrotron were provided by BioStruct-X. R.S. acknowledges the support from the Herbert and Sharon Glazer Fund Excellence Award. The cryo-TEM work was performed in the Technion Center for Electron Microscopy of Soft Matter, supported by the Technion Russell Berrie Nanotechnology Institute.

1. Chang K-J, Redmond SA, Chan JR (2016) Remodeling myelination: Implications for mechanisms of neural plasticity. *Nat Neurosci* 19:190–197.
2. Embry AF (2004) The multiple factors of multiple sclerosis: A Darwinian perspective. *J Nutr Environ Med* 14:307–317.
3. Martenson RE (1992) *Myelin—Biology and Chemistry* (CRC Press, Boca Raton, FL).
4. Snaidero N, Simons M (2014) Myelination at a glance. *J Cell Sci* 127:2999–3004.
5. Wood DD, Moscarello MA (1984) Is the myelin membrane abnormal in multiple sclerosis? *J Membr Biol* 79:195–201.
6. Bakhti M, et al. (2013) Loss of electrostatic cell-surface repulsion mediates myelin membrane adhesion and compaction in the central nervous system. *Proc Natl Acad Sci USA* 110:3143–3148.
7. Aggarwal S, et al. (2013) Myelin membrane assembly is driven by a phase transition of myelin basic proteins into a cohesive protein meshwork. *PLoS Biol* 11:e1001577.
8. Ozgen H, Baron W, Hoekstra D, Kahya N (2016) Oligodendroglial membrane dynamics in relation to myelin biogenesis. *Cell Mol Life Sci* 73:3291–3310.
9. Sospedra M, Martin R (2005) Immunology of multiple sclerosis. *Annu Rev Immunol* 23: 683–747.
10. Genain CP, Cannella B, Hauser SL, Raine CS (1999) Identification of autoantibodies associated with myelin damage in multiple sclerosis. *Nat Med* 5:170–175.
11. Ohler B, et al. (2004) Role of lipid interactions in autoimmune demyelination. *Biochim Biophys Acta* 1688:10–17.
12. Weissert R (2013) The immune pathogenesis of multiple sclerosis. *J Neuroimmune Pharmacol* 8:857–866.
13. Goldberg P (1974) Multiple sclerosis: Vitamin D and calcium as environmental determinants of prevalence. *Int J Environ Stud* 6:121–129.
14. Ransohoff RM (2012) Animal models of multiple sclerosis: The good, the bad and the bottom line. *Nat Neurosci* 15:1074–1077.
15. Hafler DA (2004) Multiple sclerosis. *J Clin Invest* 113:788–794.
16. Shaharabani R, et al. (2016) Structural transition in myelin membrane as initiator of multiple sclerosis. *J Am Chem Soc* 138:12159–12165.
17. Min Y, et al. (2009) Interaction forces and adhesion of supported myelin lipid bilayers modulated by myelin basic protein. *Proc Natl Acad Sci USA* 106:3154–3159.
18. Williams KA, Deber CM, Klrschner OA (1993) The structure and function of central nervous system myelin. *Crit Rev Clin Lab Sci* 30:29–64.
19. Inouye H, Kirschner DA (1988) Membrane interactions in nerve myelin: II. Determination of surface charge from biochemical data. *Biophys J* 53:247–260.
20. Hu Y, et al. (2004) Synergistic interactions of lipids and myelin basic protein. *Proc Natl Acad Sci USA* 101:13466–13471.
21. Luo X, et al. (2007) Cytoplasmic domain of human myelin protein zero likely folded as beta-structure in compact myelin. *Biophys J* 92:1585–1597.
22. Seddon JM (1990) Structure of the inverted hexagonal (HII) phase, and non-lamellar phase transitions of lipids. *Biochim Biophys Acta* 1031:1–69.
23. Tate MW, Gruner SM (1989) Temperature dependence of the structural dimensions of the inverted hexagonal (HII) phase of phosphatidylethanolamine-containing membranes. *Biochemistry* 28:4245–4253.
24. Caffrey M (1985) Kinetics and mechanism of the lamellar gel/lamellar liquid-crystal and lamellar/inverted hexagonal phase transition in phosphatidylethanolamine: A real-time X-ray diffraction study using synchrotron radiation. *Biochemistry* 24:4826–4844.
25. Li X, Schick M (2000) Theory of lipid polymorphism: Application to phosphatidylethanolamine and phosphatidylserine. *Biophys J* 78:34–46.
26. Li X, Schick M (2001) Theory of tunable pH-sensitive vesicles of anionic and cationic lipids or anionic and neutral lipids. *Biophys J* 80:1703–1711.
27. Ohki S, Ohshima H (1999) Interaction and aggregation of lipid vesicles (DLVO theory versus modified DLVO theory). *Colloids Surf B Biointerfaces* 14:27–45.
28. Andelman D (1995) Electrostatic properties of membranes: The Poisson-Boltzmann theory. *Handbook of Biological Physics*, eds Lipowsky R, Sackmann E (Elsevier, Amsterdam), pp 603–642.
29. Poon WCK, Andelman D (2006) *Soft Condensed Matter Physics in Molecular and Cell Biology*, eds Poon WCK, Andelman D (Taylor and Francis, New York).
30. Harries D, Raviv U (2014) Soft matter physics of lipid membrane–Based assemblies. *Liposomes, Lipid Bilayers and Model Membranes: From Basic Research to Application*, ed Pabst G, Kucerka N, Nieh M-P, Katsaras J (CRC Press, Boca Raton, FL), pp 3–30.
31. Israelachvili JN (2011) *Intermolecular and Surface Forces* (Elsevier, Santa Barbara, CA), 3rd Ed.
32. Markovich T, Andelman D, Podgornik R (2016) Charged membranes: Poisson-Boltzmann theory, DLVO paradigm and beyond. *Handbook of Lipid Membranes*, ed Safinya CRRJ (Taylor and Francis, Boca Raton, FL).
33. Kanduč M, Moazzami-Gudarzi M, Valmacco V, Podgornik R, Trefalt G (2017) Interactions between charged particles with bathing multivalent counterions: Experiments vs. dressed ion theory. *Phys Chem Chem Phys* 19:10069–10080.
34. Markovich T, Andelman D, Podgornik R (2016) Charge regulation: A generalized boundary condition? *Europhysics Lett* 113:26004.
35. Ziblat R, Leiserowitz L, Addadi L (2010) Crystalline domain structure and cholesterol crystal nucleation in single hydrated DPPC:cholesterol:POPC bilayers. *J Am Chem Soc* 132:9920–9927.
36. Kandel ER, Schwartz JH, Jessell TM (2000) *Principles of Neural Science* (McGraw-Hill, New York), 4th Ed.
37. Bakhti M, Aggarwal S, Simons M (2014) Myelin architecture: Zippering membranes tightly together. *Cell Mol Life Sci* 71:1265–1277.
38. Erickson JR, et al. (2013) Diabetic hyperglycaemia activates CaMKII and arrhythmias by O-linked glycosylation. *Nature* 502:372–376.
39. Yermolaieva O, Leonard AS, Schnizler MK, Abboud FM, Welsh MJ (2004) Extracellular acidosis increases neuronal cell calcium by activating acid-sensing ion channel 1a. *Proc Natl Acad Sci USA* 101:6752–6757.
40. Hrabcová D, Pásek M, Šimurda J, Christé G (2013) Effect of ion concentration changes in the limited extracellular spaces on sarcolemmal ion transport and Ca^{2+} turnover in a model of human ventricular cardiomyocyte. *Int J Mol Sci* 14:24271–24292.
41. Okorodudu AO, Adegboyega PA, Scholz CI (1995) Intracellular calcium and hydrogen ions in diabetes mellitus. *Ann Clin Lab Sci* 25:394–401.
42. Vitvitsky VM, Garg SK, Keep RF, Albin RL, Banerjee R (2012) Na^+ and K^+ ion imbalances in Alzheimer's disease. *Biochim Biophys Acta* 1822:1671–1681.
43. Woods LM, et al. (2016) Materials perspective on Casimir and van der Waals interactions. *Rev Mod Phys* 88:45003.
44. Dean DS, Dobnikar J, Naji A, Podgornik R (2014) *Electrostatics of Soft and Disordered Matter* (CRC Press, Boca Raton, FL).
45. Sinha S, Jing H, Das S (2017) Charge inversion and external salt effect in semipermeable membrane electrostatics. *J Membr Sci* 533:364–377.
46. Taheri-Araghi S, Ha B-Y (2005) Charge renormalization and inversion of a highly charged lipid bilayer: Effects of dielectric discontinuities and charge correlations. *Phys Rev E Stat Nonlin Soft Matter Phys* 72:021508.
47. Marcelja S (1992) Electrostatics of membrane adhesion. *Biophys J* 61:1117–1121.
48. Rouzina I, Bloomfield VA (1996) Macroion attraction due to electrostatic correlation between screening counterions. 1. Mobile surface-adsorbed ions and diffuse ion cloud. *J Phys Chem* 100:9977–9989.
49. Lis LJ, Lis WT, Parsegian VA, Rand RP (1981) Adsorption of divalent cations to a variety of phosphatidylcholine bilayers. *Biochemistry* 20:1771–1777.
50. Lau ALY, McLaughlin AC, MacDonald RC, McLaughlin SGA (1980) The adsorption of alkaline Earth cations to phosphatidyl choline bilayer membranes: A unique effect of calcium. *Bioelectrochemistry: Ions, Surfaces, Membranes*, ed Martin B (ACS Publications, Washington, DC), pp 49–56.
51. Lotan O, Fink L, Shemesh A, Tamburu C, Raviv U (2016) Critical conditions for adsorption of calcium ions onto dipolar lipid membranes. *J Phys Chem A* 120:3390–3396.
52. Iraolagoitia XLR, Martini MF (2010) Ca^{2+} adsorption to lipid membranes and the effect of cholesterol in their composition. *Colloids Surf B Biointerfaces* 76:215–220.
53. Harauz G, Boggs JM (2013) Myelin management by the 18.5-kDa and 21.5-kDa classic myelin basic protein isoforms. *J Neurochem* 125:334–361.
54. Vassall KA, Bamm VV, Harauz G (2015) MyelStones: The executive roles of myelin basic protein in myelin assembly and destabilization in multiple sclerosis. *Biochem J* 472:17–32.
55. Haas H, et al. (2004) Small angle x-ray scattering from lipid-bound myelin basic protein in solution. *Biophys J* 86:455–460.
56. Siegel DP (1986) Inverted micellar intermediates and the transitions between lamellar, cubic, and inverted hexagonal lipid phases. II. Implications for membrane-membrane interactions and membrane fusion. *Biophys J* 49:1171–1183.
57. Cheng A, Mencke A, Caffrey M (1996) Manipulating mesophase behavior of hydrated DHPE: An X-ray diffraction study of temperature and pressure effects. *J Phys Chem* 100:299–306.
58. Hing FS, Maulik PR, Shipley GG (1991) Structure and interactions of ether- and ester-linked phosphatidylethanolamines. *Biochemistry* 30:9007–9015.
59. Szekely P, Asor R, Dvir T, Szekely O, Raviv U (2012) Effect of temperature on the interactions between dipolar membranes. *J Phys Chem B* 116:3519–3524.
60. Garcia-Manyes S, Oncins G, Sanz F (2005) Effect of temperature on the nanomechanics of lipid bilayers studied by force spectroscopy. *Biophys J* 89:4261–4274.
61. Leavitt VM, Sumowski JF, Chiaravalloti N, Deluca J (2012) Warmer outdoor temperature is associated with worse cognitive status in multiple sclerosis. *Neurology* 78: 964–968.
62. Sumowski JF, Leavitt VM (2014) Body temperature is elevated and linked to fatigue in relapsing-remitting multiple sclerosis, even without heat exposure. *Arch Phys Med Rehabil* 95:1298–1302.
63. Kirk GL, Gruner SM, Stein DL (1984) A thermodynamic model of the lamellar to inverse hexagonal phase transition of lipid membrane-water systems. *Biochemistry* 23: 1093–1102.
64. Chen Z, Rand RP (1997) The influence of cholesterol on phospholipid membrane curvature and bending elasticity. *Biophys J* 73:267–276.